

TopoFlow: Physics-guided Neural Networks for high-resolution air quality prediction

Ammar Kheder^{*1,2}, Helmi Toropainen^{2,3}, Wenqing Peng^{2,3}, Samuel Antão⁴, Jia Chen⁵, Zhi-Song Liu^{1,2}, and Michael Boy^{1,2,3}

¹Department of Computational Engineering, Lappeenranta–Lahti University of Technology LUT, Finland

²Atmospheric Modelling Centre Lahti, Lahti University Campus, Finland

³Institute for Atmospheric and Earth System Research, University of Helsinki, P.O. Box 64, Helsinki 00014, Finland

⁴Advanced Micro Devices (AMD), Munich, Germany

⁵Technical University of Munich, Munich, Germany

Abstract

We propose TopoFlow (Topography-aware pollutant Flow learning), a physics-guided neural network for efficient, high-resolution air quality prediction. To explicitly embed physical processes into the learning framework, we identify two critical factors governing pollutant dynamics: topography and wind direction. Complex terrain can channel, block, and trap pollutants, while wind acts as a primary driver of their transport and dispersion. Building on these insights, TopoFlow leverages a vision transformer architecture with two novel mechanisms: topography-aware attention, which explicitly models terrain-induced flow patterns, and wind-guided patch reordering, which aligns spatial representations with prevailing wind directions. Trained on six years of high-resolution reanalysis data assimilating observations from over 1,400 surface monitoring stations across China, TopoFlow achieves a PM_{2.5} RMSE of 9.71 $\mu\text{g}/\text{m}^3$, representing a 71–80% improvement over operational forecasting systems and a 13% improvement over state-of-the-art AI baselines. Forecast errors remain well below China’s 24-hour air quality threshold of 75 $\mu\text{g}/\text{m}^3$ (GB 3095-2012), enabling reliable discrimination between clean and polluted conditions. These performance gains are consistent across all four major pollutants and forecast lead times from 12 to 96 hours, demonstrating that principled integration of physical knowledge into neural networks can fundamentally advance air quality prediction.

Keywords: Air pollution forecasting, Neural Networks, attention, air quality, China, PM2.5

1 Introduction

Air pollution kills 8.1 million people annually, more than malaria, tuberculosis, and HIV/AIDS combined, yet forecasting systems still fail to predict, especially for pollutants that accumulate in complex terrain [1]. Besides the driving force of meteorological parameters, e.g., wind directions, topography also plays a key role in shaping surface-level exposure: mountains impede horizontal dispersion, valleys channel airflow along preferred directions, and enclosed basins trap pollutants under stable atmospheric conditions. These terrain effects have contributed to severe historical pollution events, from the 1930 Meuse Valley disaster [2] to persistent wintertime haze episodes in China’s Sichuan Basin and Guanzhong Plain [3, 4]. The governing

^{*}Corresponding author: ammar.kheder@lut.fi

physics is well established, as terrain modulates both pollutant dispersion and the near-surface wind field that drives advection [5], yet data-driven forecasting approaches typically lack explicit terrain awareness, limiting their ability to capture these effects.

Current numerical chemical transport models struggle to resolve terrain-pollution interactions. Global systems, such as CAMS, operate at approximately 0.75° resolution, insufficient to capture valley-scale circulations and basin confinement occurring at 10 to 50 km scales [6]. Regional systems like CUACE achieve $\text{PM}_{2.5}$ errors of 34 to 48 $\mu\text{g}/\text{m}^3$ at 24-hour lead time, representing 45–64% of China’s regulatory threshold (75 $\mu\text{g}/\text{m}^3$, GB 3095-2012) [7], due to coarse grids, uncertain emissions, and computational constraints [8, 9], with systematic errors persisting over mountainous western China and the Tibetan Plateau [10]. Even WRF-Chem, the most widely used regional model in China, shows that basin topography alone can enhance $\text{PM}_{2.5}$ concentrations by up to 12% [11], yet exhibits substantial forecast biases that require combined data assimilation and deep-learning correction to reduce RMSE by 28–62% [12]. Unlike benchmark-driven computer vision tasks where marginal gains have limited practical significance, air quality forecasting is a domain where each improvement directly translates to public health outcomes: earlier advisories, better hospital preparedness, and lives saved.

Recent AI weather forecasting models [13–16] rival numerical prediction at orders of magnitude lower computational cost, achieving comparable results. However, only a few works have studied the air pollution predictions thoroughly. Furthermore, they have not explicitly optimized the neural network architectures to learn physical constraints. For instance, built on the vision transformer [17], ClimaX relies on generic attention mechanisms that learn the spatial correlations from the large-scale training data. Some approaches model station measurements as graphs and approximate the air pollution prediction as ODE systems without considering physical constraints [20–22]. No existing method embeds the physical relationship between terrain geometry and atmospheric transport directly into the model architecture.

In this work, we are interested in encoding physical constraints into the neural networks explicitly for accurate air pollution prediction. Particularly, we focus on two physical factors: 1) terrain imposes directionally asymmetric transport where downslope dispersion is favored over upslope advection, and 2), pollutants follow wind streamlines rather than arbitrary spatial patterns. Our keen focus is high-resolution air pollution prediction (15 km \times 15 km), hence we choose vision transformer [17] among many network architectures. The reason is that it can encode the 2D map as localized patch tokens for global feature extraction via the attention [19]. Based on that, we introduce two novel mechanisms: wind-guided patch reordering, which aligns grid cells (patch tokens) with dominant advective directions, and topography-aware attention, which encodes altitude differences as flow barriers within the attention computation. We denote it as TopoFlow, topography-aware pollutant Flow learning. Using six years of high-resolution air quality reanalysis dataset over China [24], we show that TopoFlow achieves the RMSE of 9.71 $\mu\text{g}/\text{m}^3$ on $\text{PM}_{2.5}$ prediction, representing a 71 to 80% improvement over operational systems (CAMS, CUACE) and 13% improvement over state-of-the-art AI baselines including ClimaX [13] and AirCast [23]. During the severe November 2018 Beijing haze episode, TopoFlow reduces error by 92% compared to CAMS, with transport dynamics independently validated by Lagrangian trajectory analysis [37]. These results demonstrate that embedding physical constraints into the network architecture design enables accurate prediction of geography-atmosphere interactions that both numerical models and existing deep learning approaches fail to capture.

2 Results

Model design and experimental setting

The TopoFlow is proposed as a physics-guided Vision Transformer for multi-pollutant air quality forecasting. The model significantly improves the Transformer architecture [13, 17, 18] to learn spatiotemporal feature correlations for pollution forecasting (Fig. 1).

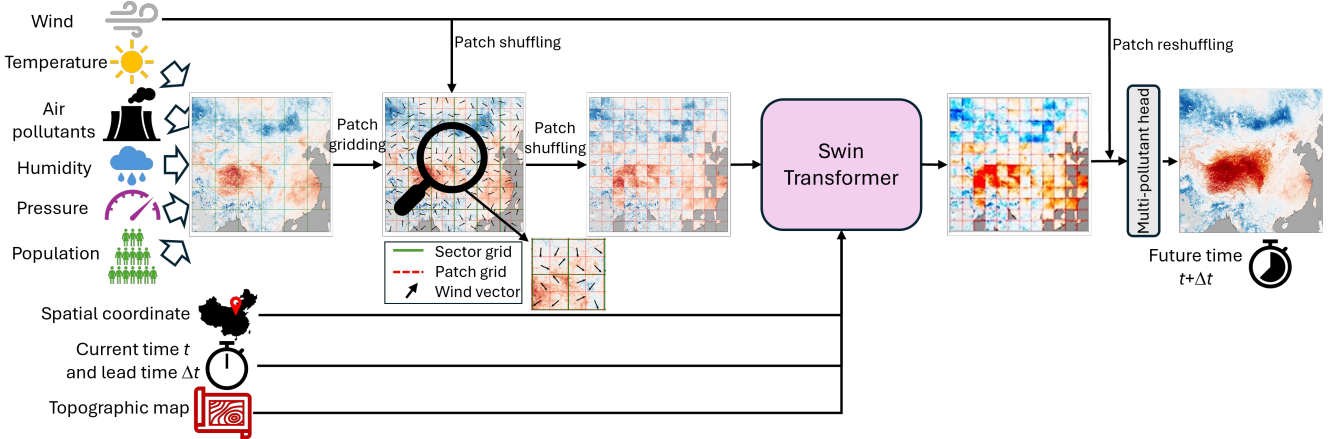


Figure 1: **TopoFlow architecture for physics-guided air quality prediction.** The model takes as input concentrations of six air pollutants, major meteorological data, population density, spatial coordinates, time stamps, and a topographic map, and outputs pollutant concentrations at lead times from 12 to 96 hours. All input data are stacked into a multi-layer 2D map, then cropped into non-overlapping patches. TopoFlow shuffles patch order based on the wind field within each sector, then processes patches through a Swin Transformer backbone. The topographic map introduces attention bias for topography-aware feature representation.

Originally, the vision transformer takes the input 2D map, which is cropped into patches and sorted in raster order, then processed via the attention mechanism for global feature extraction. Our key innovation contains two parts: (1) *wind-guided patch reordering* to align patch sequences with the wind field, whose physical motivation from advection-dominated transport theory is detailed in Appendix A, and (2) *topography-aware attention bias* to incorporate terrain-induced flow barriers.

For wind-guided patch reordering, we crop the input data into regional sectors. Within each sector, we further crop into smaller patches. The patch order within each sector is determined by the wind direction (see Algorithm B1 in Appendix B), and the attention block aligns the patches with the winds for physics-biased learning. For topography-aware attention bias, the topographic map is used as a physical bias to weight different regions based on elevation. This bias is inserted into the attention calculation to penalize high-altitude regions with less influence on pollution transport.

TopoFlow operates on a 128×256 spatial grid at 0.25° resolution covering China, forecasting six pollutants (PM_{2.5}, PM₁₀, SO₂, NO₂, CO, O₃) with resolution $15 \text{ km} \times 15 \text{ km}$ at four horizons (+12h, +24h, +48h, +96h). The model input is a multivariate spatiotemporal field $\mathbf{X} \in \mathbb{R}^{H \times W \times V_{\text{in}}}$ with $H = 128$, $W = 256$, and $V_{\text{in}} = 15$, comprising: meteorological fields (5 variables: horizontal wind u and v , temperature, relative humidity, surface pressure), pollutant concentrations (6 species, from CAQRA reanalysis [24]), spatial coordinates (latitude, longitude), and static geographic features (topography, population density); a complete specification of all input variables is provided in Supplementary Table 1.

We use the reanalysis data from the Chinese Air Quality Reanalysis (CAQRA) [24] covering China from 2013 to 2018. Topographic data is obtained from ETOPO1 [25]. Besides these, we also add the mean population density from the Gridded Population of the World dataset [26]. All meteorological and pollutant fields are standardized using z -score normalization [28] based on training statistics, while elevation and population are normalized to range $[0, 1]$ (Supplementary Section 1.1 details all preprocessing and normalization steps). The dataset is split temporally: 2013 to 2016 for training, 2017 for validation, and 2018 for testing (Supplementary Table 4 details the test set sample distribution across seasons, times of day, and days of the month). To evaluate generalization to independent observations, we additionally validate against 637 surface monitoring stations from the OpenAQ network [27] across China for 2019, ensuring complete separation between training data and evaluation.

The model contains 52.5 million learnable parameters (see Supplementary Table 3 for the complete hyperparameter configuration). We train TopoFlow for 60 epochs (20,000 optimization steps) on 128 AMD MI250X GPUs hosted on the LUMI supercomputer¹ with a batch size of 512, completing in approximately 8 days (Supplementary Section 1.2 provides full computational infrastructure details).

Multi-pollutant forecasting performance

In this section, we evaluate the performance of TopoFlow by comparing it against state-of-the-art machine learning models and operational forecasting systems (Fig. 2).

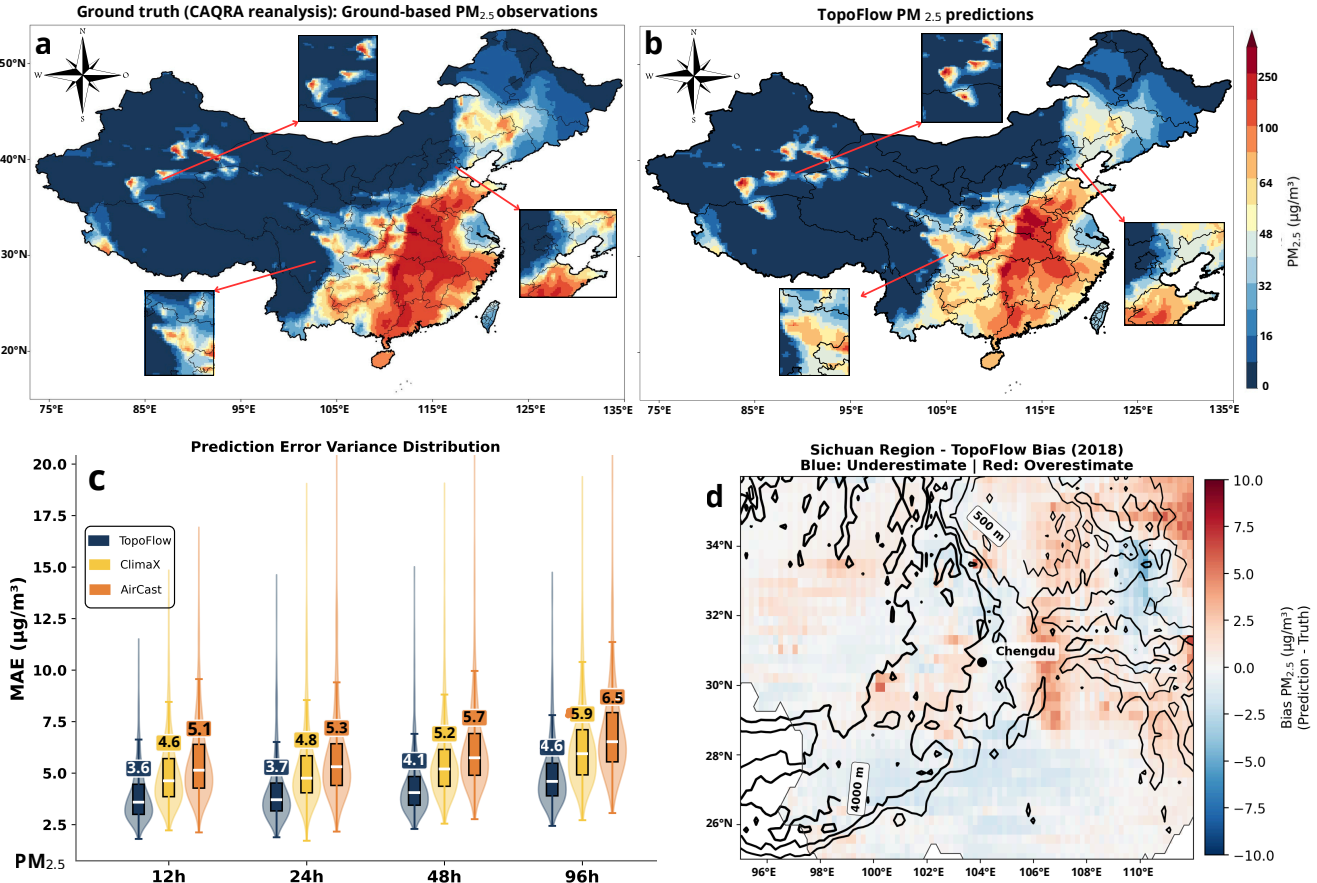


Figure 2: Overall performance of air pollution prediction. (a), Ground truth (CAQRA reanalysis) PM_{2.5} observations. (b), TopoFlow PM_{2.5} predictions. (c), Prediction error ($|\hat{y} - y|$, where \hat{y} is the model prediction and y the CAQRA reanalysis) distribution across lead times comparing TopoFlow, ClimaX, and AirCast. Box plots indicate median (middle line), 25th and 75th percentile (box), and 5th and 95th percentile (whiskers). (d), Spatial distribution of TopoFlow bias in Sichuan (with complex terrains), showing underestimation (blue) in the basin interior and overestimation (red) near elevated margins, consistent with residual difficulty in resolving sharp terrain-induced concentration gradients at the plateau-basin interface.

TopoFlow was trained on CAQRA, a 6-year high-resolution (15 km) gridded dataset that assimilates surface observations from over 1,400 monitoring stations operated by the China National Environmental Monitoring Center (CNEMC). To ensure a fair comparison, ClimaX and AirCast were trained on the same CAQRA training data (2013–2016) as TopoFlow, while Aurora was pre-trained on ERA5 and CAMS

¹<https://lumi-supercomputer.eu/>

reanalysis [16] (Supplementary Table 2). TopoFlow achieves $\text{PM}_{2.5}$ RMSE of $9.71 \mu\text{g}/\text{m}^3$, representing 13% improvement over ClimaX ($11.16 \mu\text{g}/\text{m}^3$) and 21% improvement over AirCast ($12.25 \mu\text{g}/\text{m}^3$). Similar performance gains are observed for PM_{10} , where TopoFlow ($17.25 \mu\text{g}/\text{m}^3$) outperforms all baselines. For nitrogen dioxide (NO_2) and sulfur dioxide (SO_2), TopoFlow demonstrates particularly strong performance at shorter lead times, with RMSE values of $7.79 \mu\text{g}/\text{m}^3$ and $1.44 \mu\text{g}/\text{m}^3$ at 12-hour forecasts, respectively. A comprehensive breakdown across all pollutants and lead times is provided in Supplementary Tables 5–6.

Validation against independent ground measurements

We validated TopoFlow forecasts against 637 independent surface monitoring stations from the OpenAQ network across China for 2019 (Fig. 3).

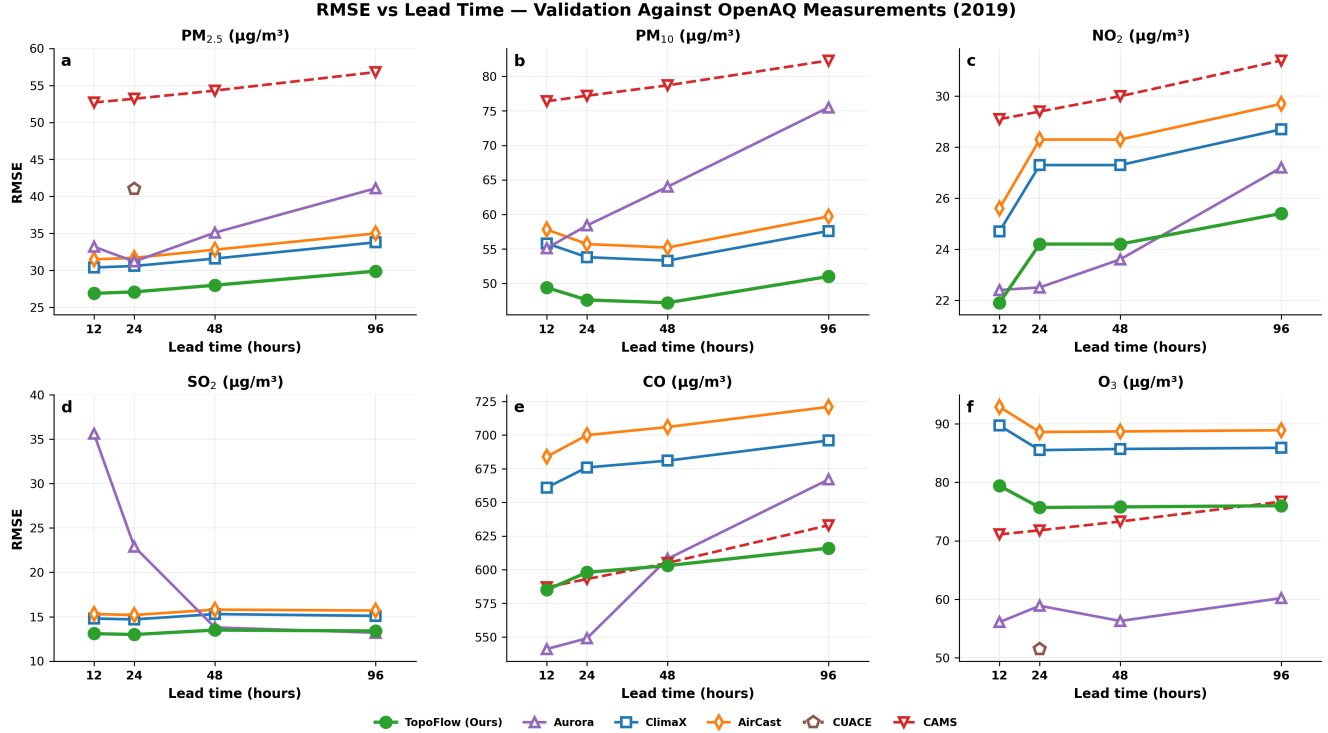


Figure 3: **Forecast skill as a function of lead time for six air pollutants.** RMSE validated against OpenAQ stations across China for 2019. **a**, $\text{PM}_{2.5}$. **b**, PM_{10} . **c**, NO_2 . **d**, SO_2 . **e**, CO . **f**, O_3 . TopoFlow (green) achieves the lowest errors for particulate matter and NO_2 . Aurora (purple) shows superior performance for O_3 and CO , which require three-dimensional atmospheric representation to capture stratospheric intrusions and vertical transport.

This strategy ensures complete separation between training data (CAQRA reanalysis) and evaluation data (direct observations), providing an unbiased assessment of real-world forecast skill. We compared TopoFlow against five established systems: Aurora [16], the state-of-the-art AI foundation model for Earth system prediction; ClimaX [13], a climate foundation model; AirCast [23], a deep learning approach for air quality; and two operational numerical chemistry systems, CAMS from ECMWF [29] and CUACE from the China Meteorological Administration [8, 9]. A detailed comparison of model architectures, training data, and physics representations is provided in Supplementary Table 2.

TopoFlow achieves the lowest errors for particulate matter ($\text{PM}_{2.5}$, PM_{10}), nitrogen dioxide (NO_2), and sulfur dioxide (SO_2) across all forecast horizons from 12 to 96 hours. For $\text{PM}_{2.5}$, TopoFlow maintains RMSE values between 27 and $30 \mu\text{g}/\text{m}^3$, representing 22% improvement over ClimaX and 45%

improvement over CAMS. Across all species, TopoFlow errors remain below 20% of the corresponding GB 3095-2012 regulatory thresholds [7] (Supplementary Table 7), whereas CAMS errors for SO_2 and PM_{10} approach or exceed half of their respective limits (Supplementary Table 7). Aurora demonstrates superior skill for ozone (O_3) and CO, achieving RMSE values approximately 25% lower than TopoFlow. This performance gap reflects architectural differences as well as the longer atmospheric lifetimes of ozone and CO compared to PM, NO_2 , and SO_2 : longer-lived species are governed by large-scale transport that Aurora captures through its three-dimensional multi-pressure-level representation, whereas short-lived pollutants are dominated by local emissions and terrain-driven dispersion where TopoFlow’s surface-level physics guidance excels.

Volatile organic compounds (VOCs) and nitrogen oxides (NO_x) are central to tropospheric ozone chemistry. Surface ozone concentrations depend on photochemical production through NO_x -VOC interactions, but are also influenced by stratospheric intrusions where ozone-rich stratospheric air descends through tropopause folding to the surface [31, 32]. These intrusions contribute 5 to 15% of tropospheric ozone and are pronounced over mountainous terrain [33, 34]. Similarly, CO undergoes vertical redistribution through deep convection during monsoon seasons [35, 36]. Aurora’s 3D Swin Transformer architecture captures these vertical processes explicitly [16]. TopoFlow’s superior performance on particulate matter despite using only surface data is physically interpretable: $\text{PM}_{2.5}$ and PM_{10} concentrations are predominantly determined by surface emissions, boundary layer dynamics, and horizontal advection [5, 39].

Seasonal and spatial validation

Fig. 4 compares spatial $\text{PM}_{2.5}$ predictions from four systems against ground observations across seasonal conditions.

CAMS forecasts and Aurora predictions exhibit concentration maxima exceeding $120 \mu\text{g}/\text{m}^3$ along the Himalayan foothills and North China Plain during winter and spring ((h) and (l) in Fig. 4), systematically overestimating surface concentrations consistent with previous evaluations [10, 30]. TopoFlow predictions exhibit smoother spatial fields, a characteristic shared by other AI weather models, including GraphCast [14] and Pangu-Weather [15], that arise from neural network regression under mean squared error optimization.

Quantitative validation confirms that TopoFlow achieves a mean RMSE of $25.9 \mu\text{g}/\text{m}^3$ against OpenAQ stations, outperforming CAQRA ($37.0 \mu\text{g}/\text{m}^3$), CAMS ($44.1 \mu\text{g}/\text{m}^3$), and Aurora ($49.8 \mu\text{g}/\text{m}^3$). Seasonal analysis reveals consistent advantages: winter conditions yield comparable errors between TopoFlow ($38.5 \mu\text{g}/\text{m}^3$) and CAQRA ($38.9 \mu\text{g}/\text{m}^3$), while CAMS ($51.8 \mu\text{g}/\text{m}^3$) and Aurora ($59.3 \mu\text{g}/\text{m}^3$) overestimate substantially. Spring presents challenging conditions with dust transport and biomass burning; TopoFlow ($34.2 \mu\text{g}/\text{m}^3$) reduces RMSE by 38% relative to CAQRA ($55.4 \mu\text{g}/\text{m}^3$). Summer monsoon conditions produce the lowest errors across all systems due to strong dispersion, with TopoFlow reaching $10.5 \mu\text{g}/\text{m}^3$.

Topographic blocking in Sichuan Basin

To demonstrate that TopoFlow’s topography-aware attention mechanism captures the fundamental physics of terrain-atmosphere interactions, we examine a summer pollution episode in the Sichuan Basin (Fig. 5).

The Sichuan Basin, a deep sedimentary depression in southwestern China enclosed by the Tibetan Plateau ($\sim 4,000$ m) to the west, functions as a natural trap for atmospheric pollutants where terrain-induced blocking governs pollution accumulation patterns that conventional deep learning approaches systematically fail to reproduce.

The 12-hour forecast initialized on 7 July 2018 reveals the characteristic signature of topographic blocking: concentrations exceeding $100 \mu\text{g}/\text{m}^3$ accumulate within the basin interior while clean air ($< 20 \mu\text{g}/\text{m}^3$) persists over the elevated western margins. Wind vectors indicate westerly flow at approximately 5 m/s,

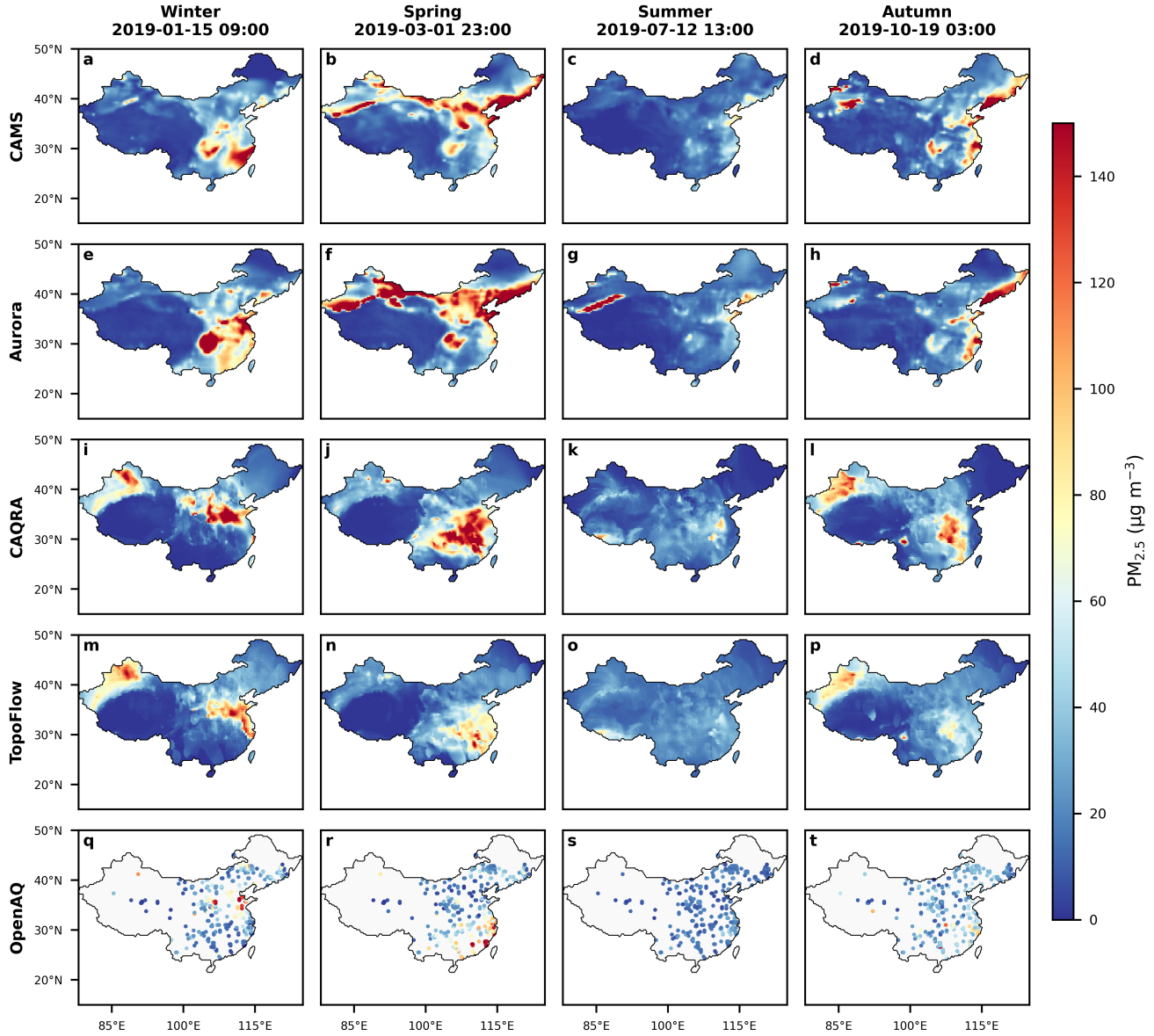


Figure 4: Seasonal PM_{2.5} distribution from forecasts, reanalysis, and observations. (a–d), CAMS forecasts. (e–h), Aurora predictions. (i–l), CAQRA reanalysis. (m–p), TopoFlow predictions. (q–t), OpenAQ measurements. Columns: Winter (15 January 2019), Spring (1 March 2019), Summer (12 July 2019), Autumn (19 October 2019). TopoFlow achieves lowest RMSE ($25.9 \mu\text{g}/\text{m}^3$) against independent stations, outperforming CAQRA ($37.0 \mu\text{g}/\text{m}^3$), CAMS ($44.1 \mu\text{g}/\text{m}^3$), and Aurora ($49.8 \mu\text{g}/\text{m}^3$). Relative to China's 24-hour PM_{2.5} threshold of $75 \mu\text{g}/\text{m}^3$ (GB 3095-2012) [7], only TopoFlow and CAQRA maintain errors below 50% of the regulatory limit.

confirming active transport conditions where clean air masses from the Tibetan Plateau encounter the basin's western rim. The west-east transect along 30.0°N provides quantitative validation: the CAQRA reanalysis PM_{2.5} profile exhibits a sharp concentration gradient $\Delta = C_{\text{basin,max}} - C_{\text{plateau,min}} = 99 \mu\text{g}/\text{m}^3$ at the elevation transition from the Tibetan Plateau to the basin floor. TopoFlow captures 77% of this gradient ($\Delta = 76 \mu\text{g}/\text{m}^3$, $r = 0.902$, RMSE = $10.3 \mu\text{g}/\text{m}^3$), while AirCast ($\Delta = 63 \mu\text{g}/\text{m}^3$, 64%) and ClimaX ($\Delta = 57 \mu\text{g}/\text{m}^3$, 58%) substantially underestimate the terrain-induced concentration discontinuity despite demonstrated skill in flat terrain. This topographic blocking extends to all six pollutants (Fig. A1):

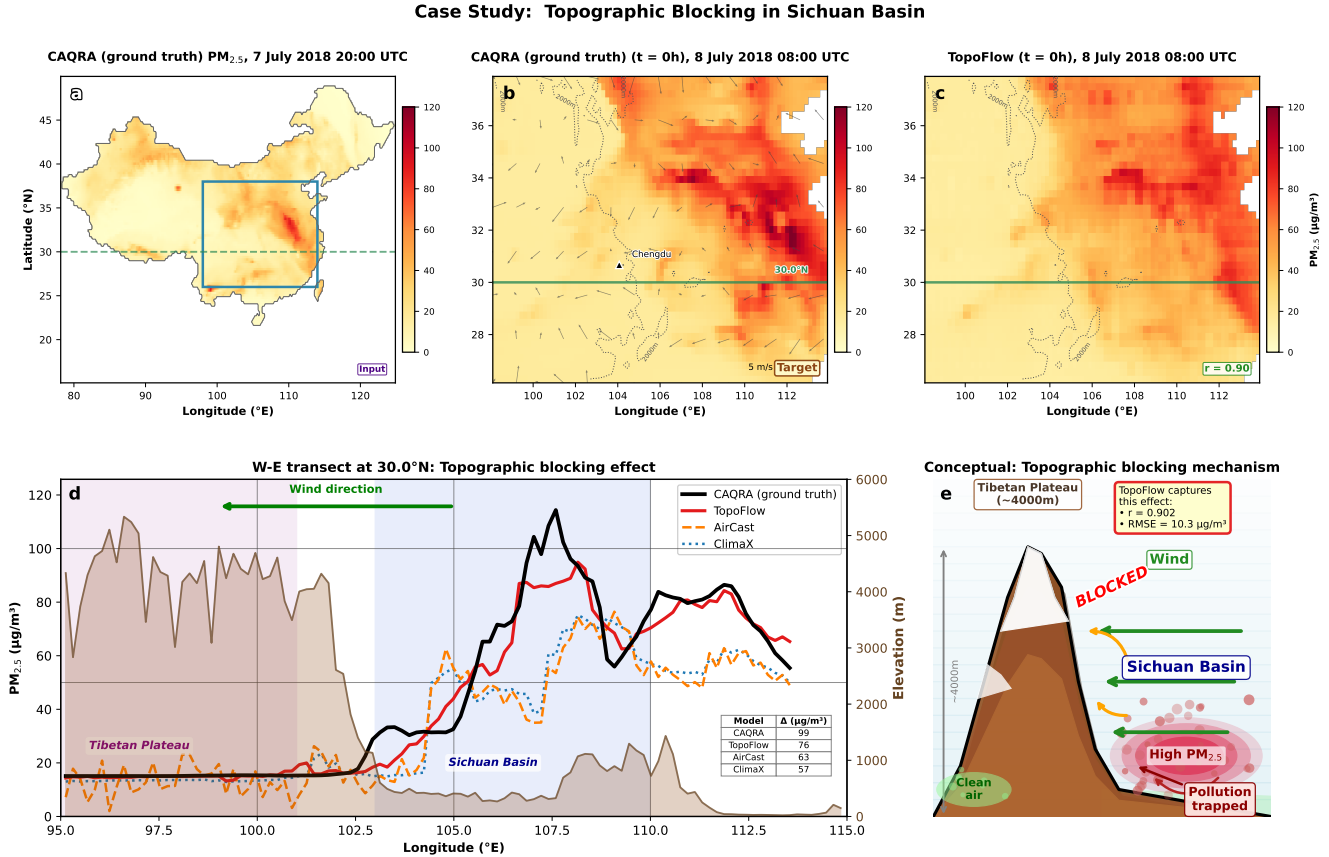


Figure 5: **Topographic blocking in Sichuan Basin.** (a), CAQRA (ground truth) PM_{2.5} distribution across China at 7 July 2018, 20:00 UTC, with the study region marked by the green box. (b), CAQRA (ground truth) PM_{2.5} concentrations and wind vectors at forecast time (8 July 2018, 08:00 UTC) within the Sichuan Basin. The green line indicates 30.0°N transect. (c), TopoFlow 12-hour prediction achieving spatial correlation $r = 0.90$. (d), West-east transect along 30.0°N comparing CAQRA (black), TopoFlow (red), AirCast (orange dashed), and ClimaX (blue dotted) against elevation profile (gray shading). Inset table reports the terrain-induced concentration gradient $\Delta = C_{\text{basin},\text{max}} - C_{\text{plateau},\text{min}}$ for each model. (e), Schematic of topographic blocking mechanism: the Tibetan Plateau blocks westerly winds, trapping pollutants within the basin.

TopoFlow captures concentration gradients for PM₁₀ ($R = 0.91$), NO₂ ($R = 0.84$), CO ($R = 0.84$), and SO₂ ($R = 0.73$), while ozone exhibits an inverse gradient consistent with nitric oxide (NO) titration within the polluted basin ($R = 0.27$).

November 2018 Beijing severe haze episode

To evaluate TopoFlow’s capacity to capture physical dynamics during extreme pollution events, we analyze the severe haze episode affecting Beijing from 11 to 15 November 2018 (Fig. 6).

This episode was characterized by PM_{2.5} concentrations exceeding 200 $\mu\text{g}/\text{m}^3$ at monitoring stations in Beijing, more than 13 times the WHO 24-hour guideline value of 15 $\mu\text{g}/\text{m}^3$ [37]. The episode was driven by a persistent blocking high-pressure system over the Beijing region, resulting in stagnant conditions with light southerly winds that allowed pollutant concentrations to accumulate over several days [37]. Using the FLEXPART-SOSAA Lagrangian modeling system, Foreback et al. [37] demonstrated that approximately 77% of particles observed in Beijing during this episode originated from outside the city, with back-trajectories indicating that up to 5% of primary particle mass and 7% of secondary organic aerosol mass

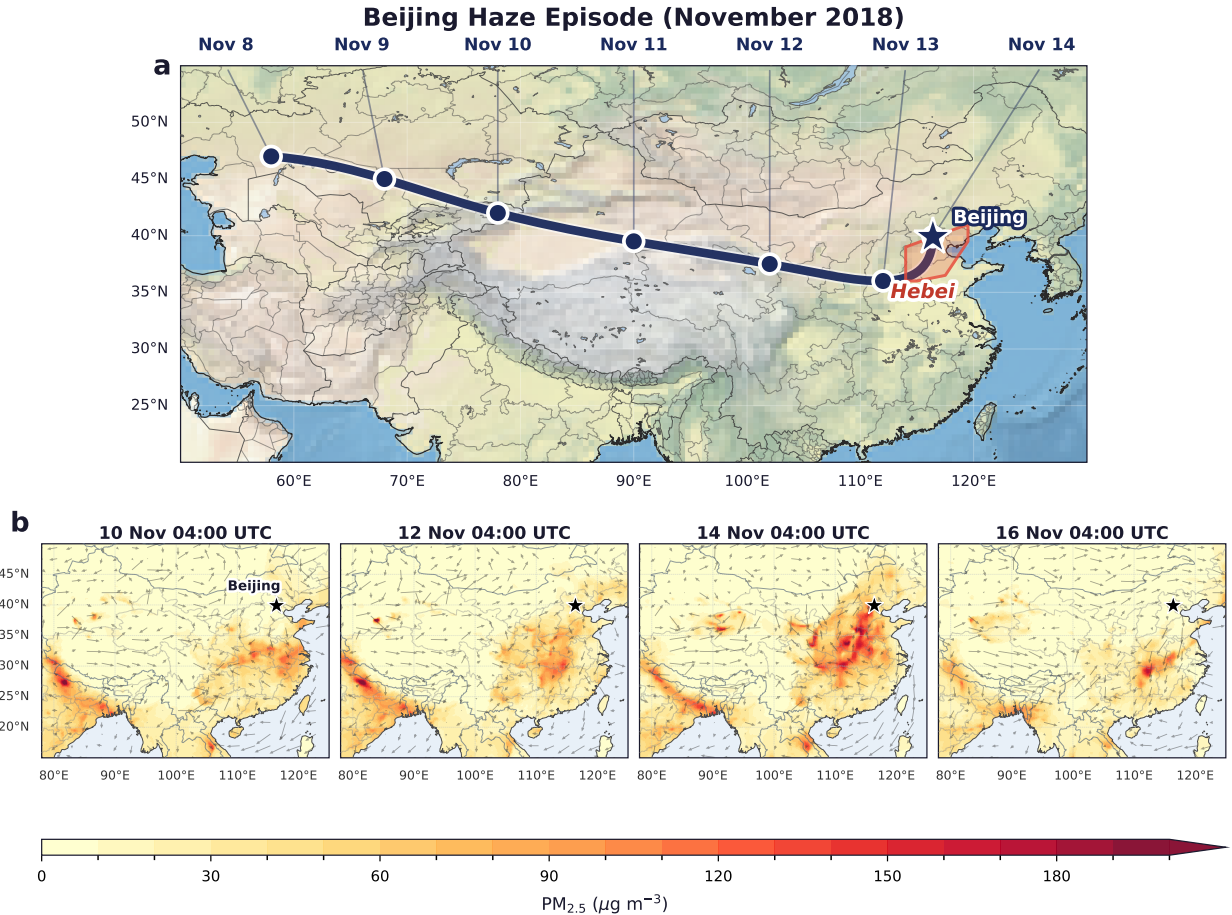


Figure 6: November 2018 Beijing haze episode. (a), Seven-day back-trajectory arriving at Beijing on 14 November 2018, adapted from FLEXPART-SOSAA analysis in Foreback et al. [37]. The trajectory originates from Central Asia and passes through the Xinjiang region before traversing Hebei province and arriving at Beijing. Dates along the trajectory indicate the air mass position at daily intervals from 8 to 14 November. (b), TopoFlow-predicted PM_{2.5} concentration fields on 10, 12, 14, and 16 November 2018 with ERA5 wind vectors overlaid. Beijing is marked with a star. The sequence shows the progressive buildup of pollution across northern China during the episode (10–14 November) and the rapid clearing on 16 November following the passage of a clean northwesterly air mass.

were transported from the Xinjiang region in western China, roughly 2000 km to the west. The trajectory arriving on 14 November (Fig. 6(a)) was classified as haze upon reaching central China, approximately three days before arriving at Beijing, and as severe haze more than one day before arrival upon entering Hebei province [37].

The TopoFlow predictions (Fig. 6(b)) capture the key spatiotemporal features of this episode independently identified by Foreback et al. [37]: the progressive accumulation of PM_{2.5} across the North China Plain during 10–14 November, the peak concentrations on 14 November extending from Hebei province into Beijing, and the abrupt clearing on 16 November when a synoptic weather shift brought clean air from the northwest. The wind vectors in panel (b) show the transition from weak, variable winds during the episode to stronger northwesterly flow during the clearing phase, consistent with the meteorological analysis in [37]. Over northern China on 14 November, TopoFlow achieves RMSE of 5.88 $\mu\text{g/m}^3$ and MAE of 3.89 $\mu\text{g/m}^3$ with correlation $r = 0.78$, compared to RMSE of 71.56 $\mu\text{g/m}^3$, MAE of 38.56 $\mu\text{g/m}^3$, and $r = 0.35$ for the operational CAMS global reanalysis [29], representing a 92% reduction in RMSE.

The independent validation by Foreback et al. [37], using an entirely different modeling framework (Lagrangian trajectory-based FLEXPART-SOSAA), different meteorological inputs (Enviro-HIRLAM and ERA5), and different emission inventories (CAMS anthropogenic and GAINS primary particle datasets), confirms that the transport patterns and source regions captured by TopoFlow reflect genuine atmospheric dynamics rather than dataset-specific artifacts.

Attention patterns reveal learned transport physics

To verify that TopoFlow’s architectural innovations translate into physically meaningful representations, we visualize attention weight matrices over the Tianshan mountain region in Xinjiang, where elevation gradients span from approximately 26 m in the Tarim Basin to 5,698 m at the mountain peaks (Fig. 7(a–c)).

The baseline architecture exhibits attention patterns uniformly distributed across all regions, indicating that most query patches attend preferentially to the same subset of key patches regardless of spatial proximity or physical relationship (Fig. 7(a)). This shortcut-like behavior routes information through a few globally informative patches, effectively ignoring local transport dynamics. The corresponding attention weight distribution is broad and left-skewed with a mean of $\mu=0.44$ (Fig. 7(d)), reflecting diffuse, unfocused information routing.

Introducing wind-guided patch reordering fundamentally restructures the attention distribution (Fig. 7(b)). By reordering patches along the dominant advective direction, sequence proximity becomes aligned with physically meaningful transport pathways. The resulting attention matrices exhibit reduced vertical striping and appears to emphasize coherent upwind source regions shared across multiple queries, indicating preferential information flow from upwind neighbors. This is reflected in a narrower, higher-mean weight distribution ($\mu=0.48$, Fig. 7(e)), consistent with more concentrated and directionally selective attention.

The full TopoFlow architecture incorporating elevation bias further refines learned attention patterns (Fig. 7(c)). The elevation-aware penalty suppresses attention weights between patches separated by large altitude differences, encoding the physical constraint that pollutants are impeded by mountain barriers. The resulting weight distribution ($\mu=0.46$, Fig. 7(f)) develops a bimodal-like structure, reflecting selective suppression of cross-barrier attention while preserving strong connectivity within topographically connected regions.

These architectural effects translate directly into improved optimization (Fig. 7(g)): TopoFlow converges to 5.7% lower validation loss than the baseline (0.249 vs. 0.264) with substantially more stable training dynamics, suggesting that embedding transport-relevant inductive biases yields a smoother optimization landscape. The individual contributions of each mechanism are quantified in the ablation study (Supplementary Table 9); Supplementary Table 8 further examines the sensitivity to tile granularity in wind-guided patch reordering: wind-guided reordering reduces validation loss by 2.7%, and adding elevation bias provides a further 3.1% reduction. Supplementary Section 2.1 provides a detailed visualization of forecast skill degradation across all four prediction horizons, showing graceful error growth from $r = 0.79$ at 12 h to $r = 0.60$ at 96 h.

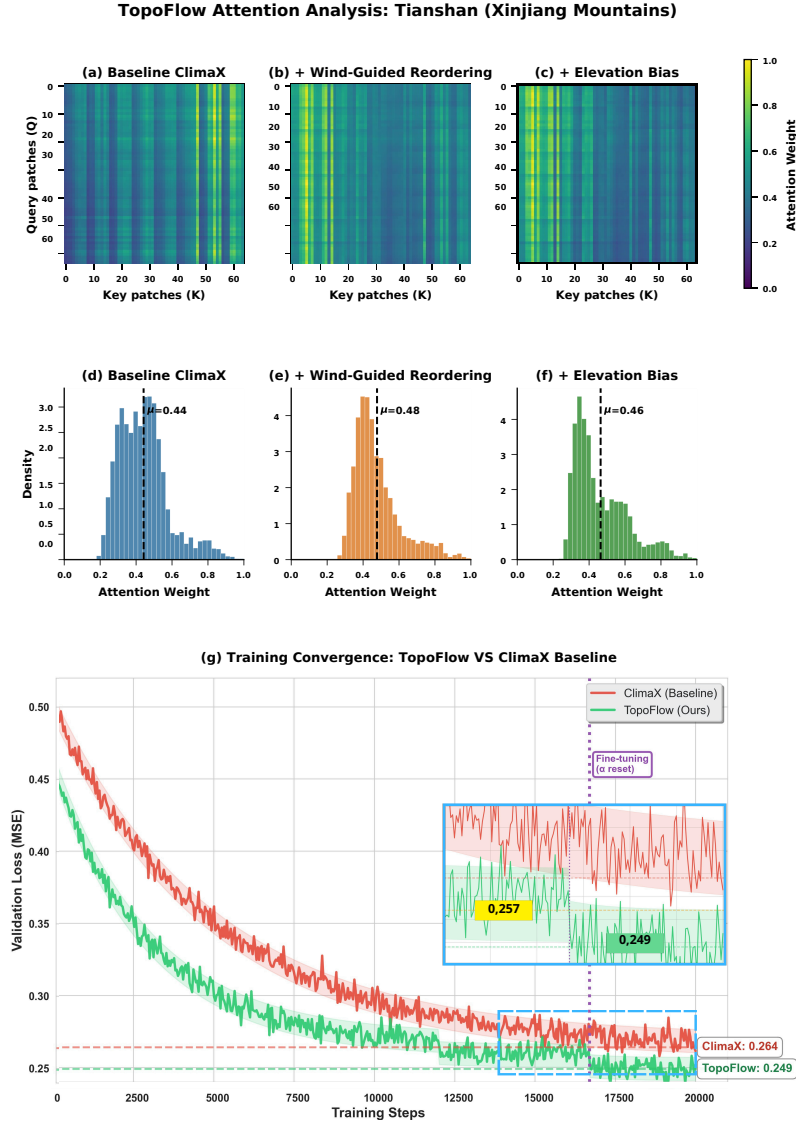


Figure 7: **Physics-guided attention learns terrain-aware transport patterns.** (a–c), Attention weight matrices over the Tianshan mountain region (elevation 26–5698 m): Baseline (a), Baseline + wind-guided patch reordering (b), and Baseline + wind-guided patch reordering + elevation bias (TopoFlow) (c). Vertical stripes in (a) indicate shortcut-like routing through globally informative patches; wind-guided reordering in (b) redistributes attention along advective transport pathways; elevation bias in (c) further modulates attention to respect topographic barriers. (d–f), Corresponding attention weight distributions with mean values μ : the baseline (d, $\mu=0.44$) shows a broad, left-skewed distribution; wind-guided reordering (e, $\mu=0.48$) concentrates weights into a narrower, higher-mean peak; the full TopoFlow model (f, $\mu=0.46$) produces a bimodal-like distribution reflecting selective suppression of cross-barrier attention. (g), Training convergence: TopoFlow achieves 5.7% lower final validation loss (0.249 vs. 0.264). The fine-tuning phase (dashed vertical line, α reset) triggers a distinct drop from 0.257 to 0.249, indicating that re-calibrating the elevation penalty after initial convergence provides an additional optimization degree of freedom absent in the baseline. Shaded regions indicate checkpoint variance.

3 Discussion

Our results demonstrate that explicitly encoding physics into the neural network, rather than treating physical constraints as loss terms [23] or additional inputs [16], fundamentally transforms air quality prediction. TopoFlow achieves $\text{PM}_{2.5}$ RMSE of $9.71 \mu\text{g}/\text{m}^3$, representing 71–80% improvement over operational systems (CAMS, CUACE) and 13% improvement over state-of-the-art AI baselines. These gains are consistent across four pollutants ($\text{PM}_{2.5}$, PM_{10} , NO_2 , SO_2) and all forecast horizons from 12 to 96 hours. The physics-guided architecture encodes domain knowledge about terrain-atmosphere interactions, enabling accurate predictions from surface data alone for species dominated by horizontal transport. The visual evidence from the mountainous area prediction Fig. 5 demonstrates that TopoFlow captures the essential physics of pollution transport: topographic blocking, wind-driven advection, and meteorological trapping. The validation in Fig. 6, using entirely different modeling frameworks and input data, demonstrates that TopoFlow has learned underlying physical dynamics rather than dataset-specific artifacts.

Attention visualization Fig. 7 also provides interpretable evidence that physics-guided mechanisms encode domain-relevant inductive biases. Wind-guided patch reordering aligns the attention mechanism with advective transport structure, while elevation bias encodes terrain barriers as constraints on information flow. These architectural modifications reduce the burden on the model to infer atmospheric transport mechanisms from data alone, yielding faster and more stable optimization.

TopoFlow’s computational efficiency relative to numerical chemistry models, combined with its interpretable physics-guided design, offers a pathway toward operational deployment in regions where complex terrain governs pollution exposure. The model processes a 96-hour forecast in under one minute on a single GPU, compared to hours for full-physics chemical transport models at comparable resolution. Supplementary Discussion provides extended analysis of operational system comparison, fair evaluation methodology, surface-only representation limitations, and generalization considerations.

Limitations and future directions

While this work has certain limitations, it also opens up several promising directions for future research. First, TopoFlow operates on surface-level data only, which limits performance for species modulated by vertical transport. Aurora’s superior skill for ozone and CO demonstrates the value of three-dimensional atmospheric representation for capturing stratospheric intrusions [31] and convective redistribution [35]. Future extensions incorporating pressure-level information may yield improvements for these species. Second, the model was trained and evaluated exclusively over China. While the physics-guided mechanisms encode general principles of terrain-atmosphere interaction, transfer to other regions with different emission patterns, meteorological regimes, or topographic configurations requires validation. The topography-aware attention and wind-guided patch reordering are architecture-level innovations that should generalize, but learned parameters may require fine-tuning. Third, TopoFlow does not currently incorporate explicit emission inventories, relying instead on the implicit emission signals captured within the CAQRA reanalysis. Integrating gridded emission datasets, such as MEIC for China, CAMS-GLOB-ANT for Europe and globally, or satellite-derived proxies, could improve the prediction of primary pollutants, particularly during emission-driven episodes. Fourth, TopoFlow currently forecasts at fixed lead times (+12h, +24h, +48h, +96h) rather than providing continuous temporal evolution. Extending to autoregressive or continuous-time formulations would enable flexible forecast horizons and uncertainty quantification through ensemble generation. Fifth, the current architecture treats all pollutants with the same physics-guided mechanisms, despite their different atmospheric lifetimes and chemical transformations. Species-specific attention biases that encode photochemical production (O_3), secondary aerosol formation (contributing to $\text{PM}_{2.5}$) or rapid oxidation (NO_2 to HNO_3) could further improve performance.

Finally, while TopoFlow demonstrates strong performance during the Beijing haze episode in November 2018, systematic evaluation across a broader range of extreme events, including dust storms, biomass

burning episodes, and industrial accidents, would strengthen confidence in operational deployment.

4 Methods

Wind-guided patch reordering

The primary mechanism in TopoFlow is patch-based attention, as proposed in Vision Transformer [17]. Let the n image patches form the matrix $\mathbf{X} = [\mathbf{x}_1, \dots, \mathbf{x}_n] \in \mathbb{R}^{n \times d}$. The core attention operation is:

$$\text{Attn}(\mathbf{X}) = \text{softmax} \left(\frac{(\mathbf{X}W_q)(\mathbf{X}W_k)^T}{\sqrt{d}} \right) (\mathbf{X}W_v) \quad (1)$$

where W_q, W_k, W_v are learnable query, key and value matrices, and d is the feature dimension. For any permutation matrix $\mathbf{P} \in \{0, 1\}^{n \times n}$, attention satisfies permutation equivariance [38]: $\text{Attn}(\mathbf{P}\mathbf{X}) = \mathbf{P}\text{Attn}(\mathbf{X})$.

We propose wind-guided patch reordering using a learned permutation matrix \mathbf{P}_w :

$$\text{Attn}(\mathbf{X}) = \text{softmax} \left(\frac{(\mathbf{P}_w\mathbf{X}W_q)(\mathbf{P}_w\mathbf{X}W_k)^T}{\sqrt{d}} \right) (\mathbf{P}_w\mathbf{X}W_v) \quad (2)$$

To compute \mathbf{P}_w , input data are divided into non-overlapping $p \times p$ patches. For each patch i , the dominant wind direction θ_{wind} is computed via magnitude-weighted averaging of local horizontal winds (u, v) :

$$\theta_{\text{wind}}^i = \arctan 2 \left(\frac{\sum_{m,n} v_{m,n} w_{m,n}}{\sum_{m,n} w_{m,n}}, \frac{\sum_{m,n} u_{m,n} w_{m,n}}{\sum_{m,n} w_{m,n}} \right), \quad w_{m,n} = \sqrt{u_{m,n}^2 + v_{m,n}^2} \quad (3)$$

We partition the domain into sectors of size $c \times r$ patches (see Appendix A for the physical motivation and Appendix B for the complete pseudocode). Within each sector, patches are sorted by their projected coordinate along the local wind direction:

$$\pi_i = x_i \cos \theta_{\text{wind}} + y_i \sin \theta_{\text{wind}} \quad (4)$$

where (x_i, y_i) is the normalized 2D coordinate of patch i . The permutation matrix \mathbf{P}_w concatenates sector-wise ordered lists. Prior to the final output layer, patches are reshuffled back to their original positions.

Topography-aware attention bias

Mountains impede atmospheric transport, making uphill advection less likely. For each patch, the mean elevation h_i is computed. The attention bias penalizes attention from patch \mathbf{x}_i to a higher-elevation patch \mathbf{x}_j :

$$\mathbf{J}_{\text{elev}}[i, j] = -\alpha \cdot \text{ReLU} \left(\frac{h_j - h_i}{h_0} \right) \quad (5)$$

where α is learnable (initialized at 2.0) and $h_0 = 1000$ m. The bias is clamped to $[-10, 0]$.

We compute the elevation embedding \mathbf{B}_{elev} via self-correlation of \mathbf{J}_{elev} . The 3D-aware attention is:

$$\mathbf{Z}_0 = \text{softmax} \left(\frac{Q_h(\mathbf{Z}_{\text{init}} + \mathbf{B}_{\text{pos}})K_h(\mathbf{Z}_{\text{init}} + \mathbf{B}_{\text{pos}})^T}{\sqrt{d}} + \mathbf{B}_{\text{elev}} \right) V_h(\mathbf{Z}_{\text{init}} + \mathbf{B}_{\text{pos}}) \quad (6)$$

where \mathbf{Z}_{init} are patch embeddings after wind-guided reordering, and $\mathbf{B}_{\text{pos}} \in \mathbb{R}^{2 \times H \times W}$ is a learnable relative 2D positional embedding.

Transformer backbone and prediction head

TopoFlow uses a stack of L transformer layers following the ViT design [17]. Each layer applies multi-head self-attention with topography and positional biases, followed by a feed-forward network with residual connections. Patch embeddings from the last transformer layer \mathbf{Z}_L are decoded by a two-layer MLP to predict patch-wise pollutant concentrations:

$$\hat{\mathbf{Y}}_{\text{patch}} \in \mathbb{R}^{N \times (V_{\text{out}} \cdot p^2)}, \quad V_{\text{out}} = 6 \quad (7)$$

Patch predictions are unpatchified and reshuffled to produce final forecasts $\hat{\mathbf{Y}} \in \mathbb{R}^{B \times V_{\text{out}} \times H \times W}$.

Training configuration

We train on 128 AMD MI250X GPUs (16 LUMI-G nodes, 8 GCDs per node) using PyTorch Lightning’s Distributed Data Parallel strategy (see Supplementary Table 3 for the complete hyperparameter configuration). The global batch size is 512. We use AdamW optimizer with weight decay $\lambda = 0.01$ and differentiated learning rates: 1×10^{-5} for pre-trained ViT blocks, 2×10^{-4} for wind-aware patch embedding, 5×10^{-5} for prediction head, and 1×10^{-4} base rate. Learning rate follows cosine annealing with 2,000-step linear warmup, decaying to $\eta_{\text{min}} = 1 \times 10^{-6}$ over 20,000 optimizer steps. Gradient clipping is applied with max norm 1.0. Training runs for 60 epochs, validating every 100 steps with early stopping (patience 10).

Loss function

TopoFlow is trained using masked mean squared error over the geographic region of China:

$$\mathcal{L} = \frac{1}{\|\mathbf{M}\|_1} \sum_{v=1}^{V_{\text{out}}} \sum_{i,j} M_{i,j} \left(\hat{Y}_{v,i,j} - Y_{v,i,j} \right)^2 \quad (8)$$

where \mathbf{M} is a binary land mask covering approximately 45% of the grid. The model forecasts all horizons (+12h, +24h, +48h, +96h) simultaneously.

Evaluation protocol

Model performance is evaluated using root mean squared error (RMSE) computed separately for each pollutant and forecast horizon:

$$\text{RMSE} = \sqrt{\frac{1}{\|\mathbf{M}\|_1} \sum_{i,j} M_{i,j} \cdot \left(\hat{Y}_{i,j} - Y_{i,j} \right)^2} \quad (9)$$

All predictions and ground truth are denormalized to physical units ($\mu\text{g}/\text{m}^3$ for particulates) before computing metrics. We report results aggregated per pollutant, per forecast horizon, and per pollutant-horizon pair.

5 Data availability

The Chinese Air Quality Reanalysis (CAQRA) dataset is available at <https://doi.org/10.11922/sciencedb.00053> [24]. OpenAQ monitoring station data are publicly available at <https://openaq.org>. Elevation data (ETOPO1) is available from NOAA National Centers for Environmental Information at <https://doi.org/10.7289/V5C8276M> [25]. Population density data (Gridded Population of the World, Version

4) is available from NASA Socioeconomic Data and Applications Center (SEDAC) at <https://doi.org/10.7927/H49C6VHW> [26]. ERA5 meteorological reanalysis data are available from the Copernicus Climate Data Store at <https://cds.climate.copernicus.eu>. Source data for all figures are provided with this paper.

6 Code availability

The TopoFlow model code, training scripts, and evaluation notebooks are available at <https://github.com/AmmarKheder/TopoFlow> and <https://ammarkheder.github.io/TopoFlow/>

Acknowledgements

This work was supported by the Finnish Ministry of Education and Culture’s Pilot for Doctoral Programmes (Pilot project Mathematics of Sensing, Imaging and Modelling). We acknowledge CSC – IT Center for Science, Finland (<https://csc.fi>), for awarding this project generous access to the LUMI supercomputer, owned by the EuroHPC Joint Undertaking, hosted by CSC (Finland) and the LUMI consortium. Thanks to city of Lahti (Finland) for financial support. We thank the developers of the Chinese Air Quality Reanalysis (CAQRA) dataset for making their data publicly available.

Author contributions

A.K. conceived the study, developed the model architecture, implemented the code, performed all experiments, and wrote the manuscript. H.T. contributed to data preprocessing. W.P. assisted with experimental design. S.A. provided technical guidance for GPU optimization on AMD MI250X. J.C. contributed to the review and interpretation of atmospheric chemistry results. Z.-S.L. supervised the machine learning development, contributed to methodology development and manuscript writing. M.B. supervised the atmospheric science aspects, provided overall project direction, and secured funding. All authors reviewed and edited the manuscript.

Competing interests

S.A. is an employee of AMD. The remaining authors declare no competing interests.

Supplementary Information

Correspondence and requests for materials should be addressed to A.K. (ammar.kheder@lut.fi).

Fig. A1 extends the $\text{PM}_{2.5}$ case study (Fig. 5) to all six pollutants at 0.4° resolution. TopoFlow consistently outperforms both CAMS and Aurora across all species ($R = 0.27\text{--}0.91$), confirming that the topography-aware attention mechanism generalizes beyond particulate matter.

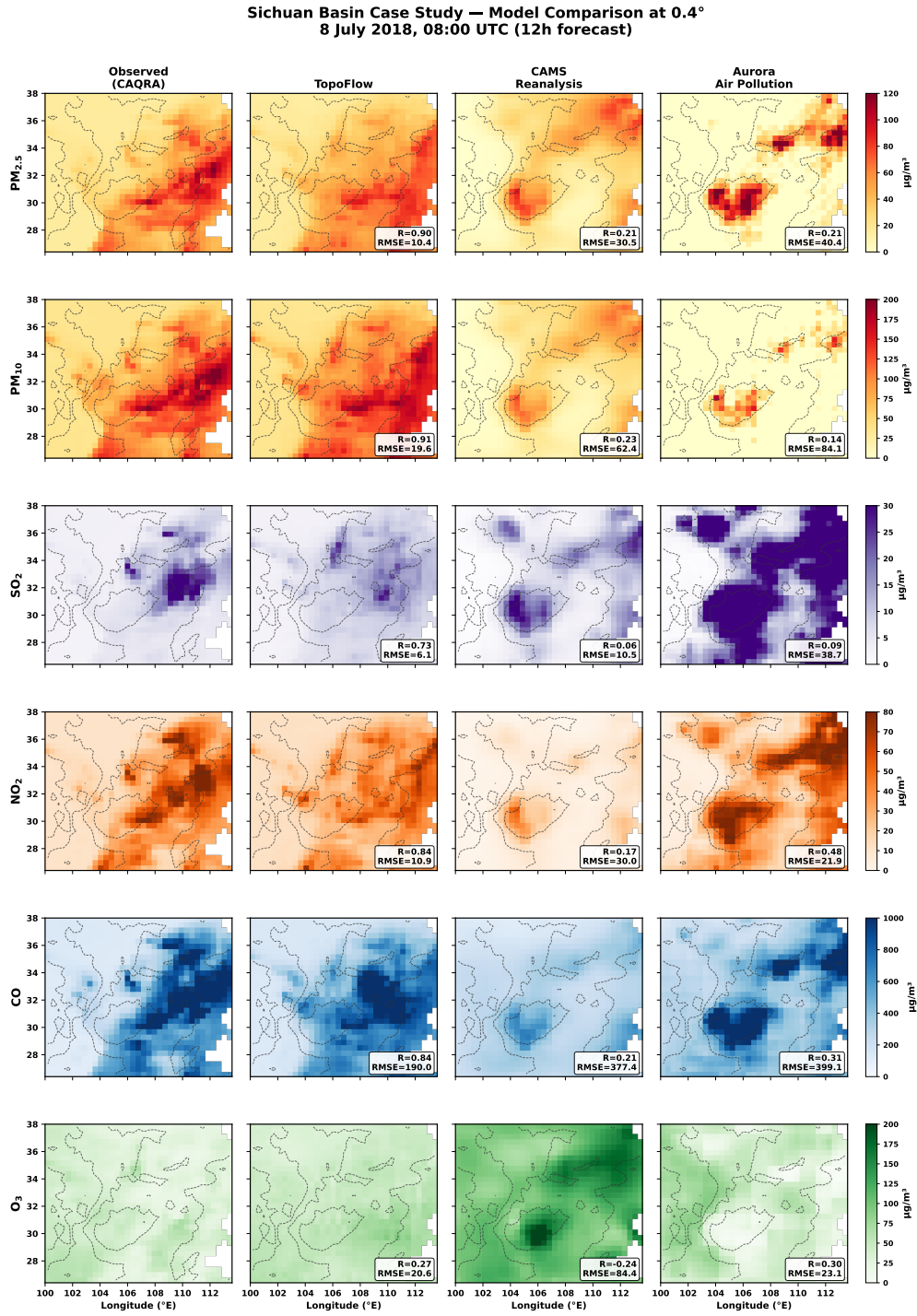


Figure 8: **Multi-pollutant model comparison over the Sichuan Basin** (8 July 2018, 08:00 UTC, 12h forecast). Rows: PM_{2.5}, PM₁₀, SO₂, NO₂, CO, O₃. Columns: CAQRA observations, TopoFlow, CAMS reanalysis, Aurora. All fields at 0.4°. R and RMSE computed against CAQRA.

A Physical Motivation of Wind-Guided Patch Reordering

A.1 Advection-dominated transport

The wind-guided patch reordering is motivated by advection-dominated transport in the atmospheric boundary layer. Consider the linear advection-diffusion-reaction equation governing pollutant concentration $c(\mathbf{x}, t)$:

$$\frac{\partial c}{\partial t} + \mathbf{u} \cdot \nabla c = \kappa \nabla^2 c + Q - D, \quad (\text{A1})$$

where \mathbf{u} is the wind velocity field, κ is the molecular diffusivity, Q represents source terms, and D represents sink terms. In the atmospheric boundary layer, the Péclet number $\text{Pe} = \|\mathbf{u}\|L/\kappa \gg 1$, implying that advection dominates diffusion. Information therefore propagates predominantly along wind streamlines rather than isotropically.

Defining the along-wind coordinate $s_i = \mathbf{x}_i \cdot \hat{\mathbf{u}}$, with $\hat{\mathbf{u}} = \mathbf{u}/\|\mathbf{u}\|$, the conditional covariance between pollutant concentrations at two locations decays exponentially along the wind direction:

$$|\text{Cov}(c_i, c_j)| \leq C \exp\left[-\gamma \frac{|s_i - s_j|}{L_{\text{adv}}}\right], \quad L_{\text{adv}} \approx \|\mathbf{u}\|\tau, \quad (\text{A2})$$

where C is a normalization constant, γ is the decay rate, and L_{adv} is the characteristic advective length scale over timescale τ . Reordering patches along s_i transforms the covariance matrix into a banded, nearly lower-triangular structure, reflecting the causal nature of advective transport.

A.2 Permutation equivariance guarantee

Standard vision transformers process patches in raster-scan order (left-to-right, top-to-bottom), which does not align with the directional structure of atmospheric transport. This mismatch forces the attention mechanism to learn long-range dependencies that are physically unnecessary.

Consider a pollution plume advecting from west to east under prevailing westerly winds. In raster-scan order, upwind (western) and downwind (eastern) patches may be separated by many tokens in the sequence, requiring the model to learn complex attention patterns to capture what is fundamentally a local upwind–downwind relationship. By reordering patches along the wind direction, these physically related patches become adjacent in the sequence, simplifying the required attention structure.

A key property of multi-head self-attention is its permutation equivariance. For any permutation matrix \mathbf{P}_w and input sequence \mathbf{X} :

$$\mathbf{P}_w^{-1} \cdot \text{Attn}(\mathbf{P}_w \mathbf{X}) = \text{Attn}(\mathbf{X}),$$

where $\text{Attn}(\cdot)$ denotes multi-head self-attention with positional encoding removed. This guarantees that reordering patches before attention and inverse-reordering afterward introduces no approximation error. The practical benefit arises when combining wind-guided ordering with local attention windows or linear attention mechanisms, where only nearby tokens interact—ensuring that *nearby in sequence* corresponds to *nearby along the wind streamline*.

B Wind-Guided Patch Reordering

The sector-based wind-guided patch reordering is summarized in Algorithm B1. Patches are reordered locally within sectors rather than globally across the entire domain, which reduces computational cost from $\mathcal{O}(N \log N)$ to $\mathcal{O}(K \cdot M \log M)$, where K is the number of sectors and $M = cr$ is the number of patches per sector, while preserving mesoscale spatial structure and local wind alignment.

Algorithm B1 Wind-Guided Patch Reordering

Input: Input tensor $\mathbf{X} \in \mathbb{R}^{B \times C \times H \times W}$, wind fields (u, v)
Input: Sector size (c, r) , patch size p
Output: Reordered patches \mathbf{X}' , inverse permutation \mathbf{P}_w^{-1}

- 1: Divide domain into sectors of size $c \times r$ patches
- 2: **for** each sector s **do**
- 3: Compute mean wind components (\bar{u}_s, \bar{v}_s) within sector
- 4: Compute wind direction: $\theta_s = \arctan 2(\bar{v}_s, \bar{u}_s)$
- 5: **for** each patch i in sector s **do**
- 6: Compute projection: $\pi_i = x_i \cos \theta_s + y_i \sin \theta_s$
- 7: **end for**
- 8: Sort patches in sector s by increasing π_i
- 9: **end for**
- 10: Concatenate sector-wise permutations to form \mathbf{P}_w
- 11: Apply permutation: $\mathbf{X}' = \mathbf{P}_w \mathbf{X}$
- 12: **return** \mathbf{X}' , \mathbf{P}_w^{-1}

Supplementary Information

TopoFlow: Physics-guided Neural Networks for high-resolution air quality prediction

Ammar Kheder, Helmi Toropainen, Wenqing Peng, Samuel Antão, Jia Chen, Zhi-Song Liu, Michael Boy

Contents

1	Introduction	1
2	Results	2
3	Discussion	12
4	Methods	13
5	Data availability	14
6	Code availability	15
A	Physical Motivation of Wind-Guided Patch Reordering	17
A.1	Advection-dominated transport	17
A.2	Permutation equivariance guarantee	17
B	Wind-Guided Patch Reordering	17
S1	Supplementary Methods	20
S1.1	Data preprocessing and normalization	20
S1.2	Training infrastructure and computational cost	20
S2	Supplementary Figures	20
S2.1	Forecast skill degradation with lead time	20
S3	Supplementary Tables	22
S3.1	Input variable specification	22
S3.2	Baseline model specifications	22
S3.3	Hyperparameter configuration	23
S3.4	Test set sample distribution	24
S3.5	RMSE performance by pollutant and forecast horizon	24
S3.6	Validation against independent ground stations	25
S3.7	Ablation study: tile granularity	26
S3.8	Ablation study: component contributions	26
S4	Supplementary Discussion	27
S4.1	Comparison with operational forecasting systems	27
S4.2	Fair comparison with AI baselines	27
S4.3	Limitations of surface-only representation	27
S4.4	Generalization to other regions	27

S1 Supplementary Methods

S1.1 Data preprocessing and normalization

All input variables undergo careful preprocessing to ensure numerical stability and meaningful feature representations:

Meteorological variables. Horizontal wind components (u, v), temperature, relative humidity, and surface pressure are standardized using z-score normalization with statistics computed from the training set (2013–2016). This normalization preserves the physical relationships between variables while centering the data for neural network optimization.

Pollutant concentrations. The six pollutant species (PM_{2.5}, PM₁₀, SO₂, NO₂, CO, O₃) are also z-score normalized. Notably, we do not apply log-transformation despite the heavy-tailed distribution of pollution concentrations, as this would distort the relative importance of extreme events that are critical for air quality forecasting.

Static features. Elevation and population density are normalized to the range [0, 1] using min-max scaling. This ensures that the topographic attention bias operates on a consistent scale regardless of the absolute elevation range in the domain.

Temporal encoding. Time of day and day of year are encoded using sinusoidal functions to capture cyclical patterns:

$$t_{\text{hour}} = \left[\sin\left(\frac{2\pi \cdot \text{hour}}{24}\right), \cos\left(\frac{2\pi \cdot \text{hour}}{24}\right) \right]$$

$$t_{\text{doy}} = \left[\sin\left(\frac{2\pi \cdot \text{doy}}{365}\right), \cos\left(\frac{2\pi \cdot \text{doy}}{365}\right) \right]$$

S1.2 Training infrastructure and computational cost

TopoFlow was trained on the LUMI supercomputer, one of the world’s largest GPU-accelerated systems. We utilized 16 LUMI-G nodes, each equipped with 8 AMD MI250X Graphics Compute Dies (GCDs), for a total of 128 GCDs. Each MI250X GCD provides 128 GB of high-bandwidth memory (HBM2e), enabling large batch sizes essential for stable distributed training.

The training configuration employed PyTorch Lightning’s Distributed Data Parallel (DDP) strategy with the following specifications: global batch size of 512 samples (per-GPU batch size of 2 with gradient accumulation of 2), mixed precision (FP16) with dynamic loss scaling, and NCCL communication backend over Slingshot-11 interconnect. Total training time was approximately 8 days for 60 epochs. The model checkpoint with lowest validation loss was selected for final evaluation.

S2 Supplementary Figures

S2.1 Forecast skill degradation with lead time

Supplementary Figure S1 presents a comprehensive analysis of TopoFlow forecast performance across all four prediction horizons. Several patterns emerge from this analysis:

Spatial bias structure. The bias maps (panels i–l) show systematic underestimation (blue) over the North China Plain and Sichuan Basin at longer lead times. This pattern is consistent with the accumulation of forecast errors in regions where pollution episodes are driven by synoptic-scale meteorological patterns that become increasingly uncertain at extended horizons.

Correlation decay. The correlation coefficient decreases from $r = 0.79$ at 12h to $r = 0.60$ at 96h, representing a 24% reduction in linear association. However, even at 96h, the model maintains substantial predictive skill, outperforming persistence forecasts and climatological baselines.

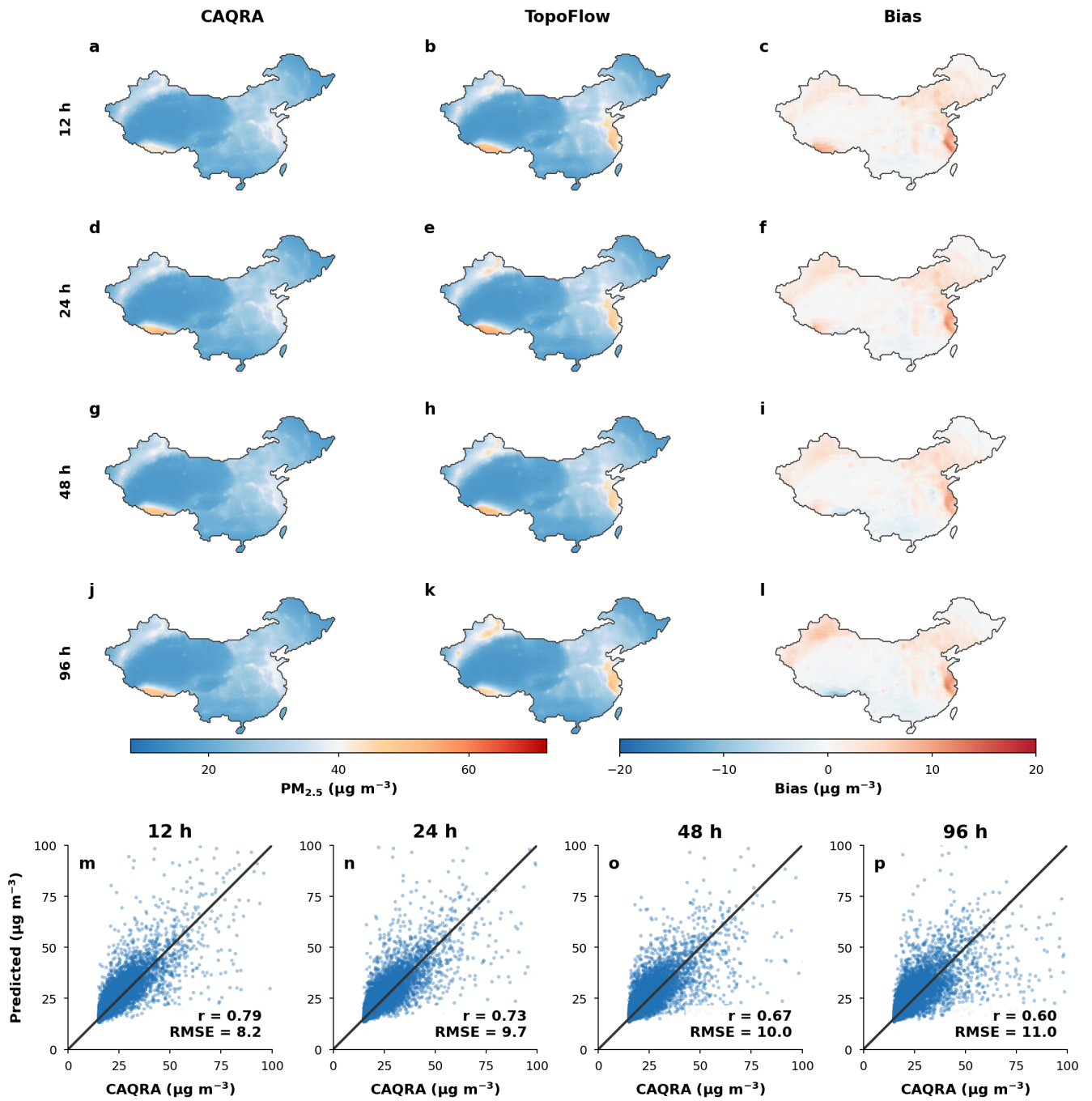


Figure S1: **TopoFlow PM_{2.5} forecast performance across lead times.** **a–d**, CAQRA reanalysis (ground truth) for 12h, 24h, 48h, and 96h horizons. **e–h**, Corresponding TopoFlow predictions. **i–l**, Spatial bias maps showing prediction minus observation (blue: underestimation, red: overestimation). **m–p**, Scatter plots of predicted versus observed PM_{2.5} concentrations with correlation coefficient r and RMSE. Performance degrades gracefully from $r = 0.79$ at 12h to $r = 0.60$ at 96h, with RMSE increasing from 8.2 to 11.0 $\mu\text{g}/\text{m}^3$.

RMSE growth. Root mean squared error increases from 8.2 $\mu\text{g}/\text{m}^3$ at 12h to 11.0 $\mu\text{g}/\text{m}^3$ at 96h, a 34% increase. This error growth rate is comparable to state-of-the-art numerical weather prediction models for similar forecast ranges.

Scatter plot characteristics. The scatter plots (panels m–p) reveal increasing spread at longer

lead times, with the point cloud becoming more diffuse around the 1:1 line. Notably, the model tends to underpredict extreme concentrations ($>75 \mu\text{g}/\text{m}^3$) at all horizons, a common characteristic of regression-based approaches trained with mean squared error loss.

S3 Supplementary Tables

S3.1 Input variable specification

Table S1: Complete specification of TopoFlow input variables.

Variable	Symbol	Units	Source	Resolution	Normalization
<i>Meteorological fields</i>					
Zonal wind	u	m/s	CAQRA	0.25°	z-score
Meridional wind	v	m/s	CAQRA	0.25°	z-score
Temperature	T	K	CAQRA	0.25°	z-score
Relative humidity	RH	%	CAQRA	0.25°	z-score
Surface pressure	p_s	hPa	CAQRA	0.25°	z-score
<i>Pollutant concentrations</i>					
PM _{2.5}	—	$\mu\text{g}/\text{m}^3$	CAQRA	0.25°	z-score
PM ₁₀	—	$\mu\text{g}/\text{m}^3$	CAQRA	0.25°	z-score
SO ₂	—	$\mu\text{g}/\text{m}^3$	CAQRA	0.25°	z-score
NO ₂	—	$\mu\text{g}/\text{m}^3$	CAQRA	0.25°	z-score
CO	—	mg/m^3	CAQRA	0.25°	z-score
O ₃	—	$\mu\text{g}/\text{m}^3$	CAQRA	0.25°	z-score
<i>Spatial coordinates</i>					
Latitude	ϕ	°	Computed	0.25°	z-score
Longitude	λ	°	Computed	0.25°	z-score
<i>Static geographic features</i>					
Elevation	h	m	ETOPO1	1 arcmin	min-max [0,1]
Population density	ρ_{pop}	persons/km ²	GPWv4	30 arcsec	min-max [0,1]

S3.2 Baseline model specifications

Table S2: Baseline model specifications and training details. ClimaX baseline and AirCast were trained on CAQRA for fair comparison.

Model	Type	Parameters	Training Data	Reference
Aurora	AI foundation model	1.3B	ERA5 + CAMS	Bodnar et al. (Nature 2025)
ClimaX baseline	Climate foundation model	100M	CAQRA	Nguyen et al. (ICML 2023)
AirCast	Deep learning	50M	CAQRA	Nedungadi et al. (ICML WS 2025)
CAMS	Numerical CTM	—	ECMWF IFS + emissions	Inness et al. (ACP 2019)
CUACE	Numerical CTM	—	CMA + MEIC emissions	Dai et al. (2019)
TopoFlow (Ours)	Physics-guided ViT	52.5M	CAQRA	This work

S3.3 Hyperparameter configuration

Table S3: Complete hyperparameter configuration for TopoFlow training.

Category	Parameter	Value
Architecture	Patch size p	2
	Embedding dimension d	768
	Number of transformer layers L	12
	Number of attention heads	8
	MLP hidden dimension	3072
Wind-guided reordering	Dropout rate	0.1
	Sector size (tiles)	32×32
	Wind averaging kernel	Magnitude-weighted
Topography-aware attention bias	Reordering frequency	Per forward pass
	Initial α	2.0
	Reference height h_0	1000 m
Optimization	Bias clamp range	$[-10, 0]$
	Optimizer	AdamW
	Weight decay λ	0.01
	Base learning rate	1×10^{-4}
	ViT blocks learning rate	1×10^{-5}
	Wind embedding learning rate	2×10^{-4}
	Prediction head learning rate	5×10^{-5}
	Warmup steps	2,000
	Total optimization steps	20,000
	LR schedule	Cosine annealing
Training	Minimum learning rate	1×10^{-6}
	Gradient clip max norm	1.0
	Global batch size	512
	Per-GPU batch size	2
	Gradient accumulation steps	2
	Number of GPUs	128 (AMD MI250X)
	Training epochs	60
	Early stopping patience	10
	Validation frequency	Every 100 steps

S3.4 Test set sample distribution

Table S4: Test set evaluation sample distribution across temporal dimensions (year 2018). Each forecast horizon contains 1,000 stratified samples covering all seasons, times of day, and days of the month.

Temporal Horizon	Seasonal Distribution				Daily Distribution				Day of Month Distribution			Total Samples
	Winter (Jan-Mar)	Spring (Apr-Jun)	Summer (Jul-Sep)	Autumn (Oct-Dec)	Night (00:00-06:00)	Morning (06:00-12:00)	Afternoon (12:00-18:00)	Evening (18:00-24:00)	Days 1-10	Days 11-20	Days 21-31	
12h	255	262	245	238	234	270	227	269	338	329	333	1,000
24h	246	225	268	261	266	227	250	257	332	327	341	1,000
48h	252	254	278	216	260	233	273	234	342	311	347	1,000
96h	255	257	239	249	272	232	254	242	344	331	325	1,000
Total	1,008	998	1,030	964	1,032	962	1,004	1,002	1,356	1,298	1,346	4,000

S3.5 RMSE performance by pollutant and forecast horizon

Table S5: RMSE performance by pollutant and forecast horizon (Test Set 2018). All units in $\mu\text{g}/\text{m}^3$. Bold indicates best performance. All models were evaluated against CAQRA reanalysis.

Pollutant	Model	12h	24h	48h	96h	Average
PM _{2.5}	TopoFlow (Ours)	8.18	9.66	9.96	11.03	9.71
	ClimaX baseline	9.41	11.11	11.45	12.68	11.16
	AirCast	10.72	12.67	12.21	13.40	12.25
PM ₁₀	TopoFlow (Ours)	14.78	17.06	17.70	19.45	17.25
	ClimaX baseline	17.00	19.62	20.36	22.37	19.84
	AirCast	17.90	20.29	19.85	21.63	19.92
SO ₂	TopoFlow (Ours)	1.44	1.49	1.48	1.75	1.54
	ClimaX baseline	1.66	1.71	1.70	2.01	1.77
	AirCast	2.89	2.88	2.81	3.27	2.96
NO ₂	TopoFlow (Ours)	7.79	7.67	7.99	8.94	8.10
	ClimaX baseline	8.96	8.82	9.19	10.28	9.31
	AirCast	9.75	9.16	9.33	10.13	9.59
CO	TopoFlow (Ours)	72.11	72.50	74.97	81.81	75.35
	ClimaX baseline	82.93	83.38	86.22	94.08	86.65
	AirCast	100.34	100.89	104.33	113.84	104.85
O ₃	TopoFlow (Ours)	14.49	12.83	14.48	15.46	14.31
	ClimaX baseline	16.66	14.75	16.65	17.78	16.46
	AirCast	24.06	19.97	21.13	21.44	21.65
Overall	TopoFlow (Ours)	19.80	20.20	21.10	22.91	21.04
	ClimaX baseline	22.77	23.23	24.26	26.53	24.20
	AirCast	27.61	27.64	28.28	30.62	28.54

S3.6 Validation against independent ground stations

Table S6: **Validation Against Independent Ground Stations (2019).** RMSE in $\mu\text{g}/\text{m}^3$. Green = TopoFlow (Ours). **Bold** = best per lead time. $\downarrow\%$ = relative increase vs. best model.

Pollutant	Model	12h	24h	48h	96h	Average	$\downarrow\%$
$\text{PM}_{2.5}$	TopoFlow (Ours)	26.9	27.1	28.0	29.9	28.0	–
	ClimaX baseline	30.4	30.6	31.6	33.8	31.6	+13%
	AirCast	31.5	31.7	32.8	35.0	32.8	+17%
	Aurora	33.2	31.2	35.1	41.1	35.2	+26%
	CUACE [†]	–	34–48	–	–	41.0	+46%
	CAMS [‡]	52.7	53.2	54.3	56.8	54.3	+94%
PM_{10}	TopoFlow (Ours)	49.4	47.6	47.2	51.0	48.8	–
	ClimaX baseline	55.8	53.8	53.3	57.6	55.1	+13%
	AirCast	57.8	55.7	55.2	59.7	57.1	+17%
	Aurora	55.1	58.4	64.0	75.5	63.3	+30%
	CAMS [‡]	76.4	77.2	78.7	82.3	78.6	+61%
SO_2	TopoFlow (Ours)	13.1	13.0	13.5	13.4	13.3	–
	ClimaX baseline	14.8	14.7	15.3	15.1	15.0	+13%
	AirCast	15.3	15.2	15.8	15.7	15.5	+17%
	Aurora	35.6	22.9	13.8	13.2	21.4	+61%
	CAMS [‡]	80.9	81.7	83.4	87.2	83.3	+526%
NO_2	TopoFlow (Ours)	21.9	24.2	24.2	25.4	23.9	–
	Aurora	22.4	22.5	23.6	27.2	23.9	0%
	ClimaX baseline	24.7	27.3	27.3	28.7	27.0	+13%
	AirCast	25.6	28.3	28.3	29.7	28.0	+17%
	CAMS [‡]	29.1	29.4	30.0	31.4	30.0	+26%
CO	Aurora	541	549	608	667	591	–
	TopoFlow (Ours)	585	598	603	616	601	+2%
	CAMS [‡]	587	593	605	633	605	+2%
	ClimaX baseline	661	676	681	696	679	+15%
	AirCast	684	700	706	721	703	+19%
O_3	CUACE[†]	–	40–63	–	–	51.5	–
	Aurora	56.1	58.9	56.3	60.2	57.9	+12%
	CAMS [‡]	71.1	71.8	73.3	76.7	73.2	+42%
	TopoFlow (Ours)	79.4	75.7	75.8	76.0	76.7	+49%
	ClimaX baseline	89.7	85.5	85.7	85.9	86.7	+68%
Mean RMSE	TopoFlow (Ours)	129.3	131.1	132.1	136.2	132.2	–
	Aurora	123.9	124.4	133.5	150.8	133.1	+0.7%
	ClimaX baseline	146.2	148.6	150.0	154.6	149.9	+13%
	CAMS [‡]	149.7	151.1	154.3	161.2	154.1	+17%
	AirCast	151.5	153.8	155.5	160.4	155.3	+17%

[†] CUACE operational values from Dai et al. (2019) and Qi et al. (2022).

[‡] CAMS forecast performance over China from Ge et al. (2020).

ClimaX baseline and AirCast were trained on CAQRA for fair comparison.

Table S7: **Forecast errors relative to China’s regulatory air quality thresholds (GB 3095-2012, Class II, 24-hour average).** RMSE from independent OpenAQ validation (2019). Values in parentheses indicate RMSE as a percentage of the regulatory threshold. Shaded cells indicate errors exceeding 50% of the threshold, limiting operational utility for regulatory decision-making.

Pollutant	Threshold	TopoFlow	ClimaX	AirCast	Aurora	CAMS
PM _{2.5}	75 $\mu\text{g}/\text{m}^3$	28.0 (37%)	31.6 (42%)	32.8 (44%)	35.2 (47%)	54.3 (72%)
PM ₁₀	150 $\mu\text{g}/\text{m}^3$	48.8 (33%)	55.1 (37%)	57.1 (38%)	63.3 (42%)	78.6 (52%)
NO ₂	80 $\mu\text{g}/\text{m}^3$	23.9 (30%)	27.0 (34%)	28.0 (35%)	23.9 (30%)	30.0 (38%)
SO ₂	150 $\mu\text{g}/\text{m}^3$	13.3 (9%)	15.0 (10%)	15.5 (10%)	21.4 (14%)	83.3 (56%)
CO*	4 mg/m^3	0.60 (15%)	0.68 (17%)	0.70 (18%)	0.59 (15%)	0.61 (15%)
O ₃	160 $\mu\text{g}/\text{m}^3$	76.7 (48%)	86.7 (54%)	—	57.9 (36%)	73.2 (46%)

* CO RMSE reported in mg/m^3 to match the regulatory threshold unit (GB 3095-2012). Values in Supplementary Tables 5–6 are reported in $\mu\text{g}/\text{m}^3$ for consistency with other pollutants.

S3.7 Ablation study: tile granularity

Table S8: Tile granularity optimization for wind-guided reordering. Validation loss on 2017 holdout set.

Tiling Strategy	Wind Calculation	Val Loss	Δ Loss
Global wind direction	Single vector (country-wide)	0.309	—
Coarse tiling	2×2 tiles	0.295	-0.014
	4×4 tiles	0.293	-0.016
Medium tiling	8×8 tiles	0.291	-0.018
	12×12 tiles	0.288	-0.021
	16×16 tiles	0.280	-0.029
Fine tiling (optimal)	32×32 tiles	0.257	-0.052
Over-parameterized	16×32 tiles	0.302	+0.007
	32×64 tiles	0.376	+0.067

The optimal tile size of 32×32 balances two competing considerations: (1) sufficient spatial extent to capture coherent wind patterns, and (2) adequate granularity to resolve mesoscale heterogeneity in the flow field. Smaller tiles lead to noisy wind estimates from insufficient averaging, while larger tiles smooth over important local variations.

S3.8 Ablation study: component contributions

Table S9: Component contribution analysis using optimal 32×32 tiles.

Model	Scanning	Wind Tiles	Elevation α	Val Loss
ClimaX baseline	Row-major	×	×	0.264
+ Wind-guided reordering	Wind-directed	32×32	×	0.257
+ Topography-aware attention bias (TopoFlow)	Wind-directed	32×32	✓	0.249

Notes: Each row adds one component to the previous configuration. Wind-guided reordering reduces validation loss by 2.7% relative to ClimaX baseline. Adding Topography-aware attention bias provides an additional 3.1% reduction. The cumulative improvement is 5.7% versus ClimaX baseline.

S4 Supplementary Discussion

S4.1 Comparison with operational forecasting systems

TopoFlow’s performance advantage over operational systems (CAMS, CUACE) stems from fundamentally different modeling approaches. Numerical chemical transport models solve the advection-diffusion equation on three-dimensional grids, requiring explicit representation of emissions, chemistry, and deposition processes. These models are computationally expensive and sensitive to errors in emission inventories, which are particularly uncertain over China.

In contrast, TopoFlow learns the mapping from current atmospheric state to future pollutant concentrations directly from reanalysis data. This data-driven approach implicitly captures emission patterns, chemical transformations, and deposition processes without requiring explicit parameterization. The physics-guided attention mechanisms ensure that learned representations respect fundamental transport constraints.

S4.2 Fair comparison with AI baselines

To ensure fair comparison, both ClimaX baseline and AirCast were trained on the same CAQRA dataset (2013–2016) with identical train/validation/test splits. This eliminates potential confounds from differences in training data quality, spatial coverage, or temporal extent. The performance improvements of TopoFlow over these baselines can therefore be attributed directly to the physics-guided architectural innovations rather than data advantages.

Aurora was not retrained on CAQRA as it is a foundation model with fixed pretrained weights. Its performance represents the zero-shot transfer capability of large-scale pretraining on global atmospheric data.

S4.3 Limitations of surface-only representation

TopoFlow’s limitation for O₃ and CO prediction reflects the importance of vertical atmospheric structure for these species. Surface ozone is influenced by stratospheric intrusions, where ozone-rich air descends through tropopause folding events. These processes are captured by Aurora’s three-dimensional representation but cannot be resolved by TopoFlow’s surface-only inputs.

Future extensions could incorporate pressure-level information from reanalysis products to capture vertical transport processes while maintaining the computational efficiency of the current architecture.

S4.4 Generalization to other regions

While TopoFlow was trained and evaluated exclusively over China, the physics-guided mechanisms encode general principles that should transfer to other regions. Wind-guided attention aligns with advective transport structure regardless of geographic location. Topography-aware attention bias encodes universal mountain meteorology principles. The transformer architecture provides flexible capacity to adapt to different pollution regimes.

However, learned parameters (attention weights, embedding layers) may require fine-tuning for regions with substantially different emission patterns, meteorological regimes, or topographic configurations.

References

- [1] Health Effects Institute. State of Global Air 2024. *Health Effects Institute Report*, Boston, MA, 2024.
- [2] Nemery, B., Hoet, P. H. M., and Nemmar, A. The Meuse Valley fog of 1930: an air pollution disaster. *The Lancet*, 357(9257):704–708, 2001.

- [3] Bei, N. et al. Typical synoptic situations and their impacts on the wintertime air pollution in the Guanzhong basin, China. *Atmospheric Chemistry and Physics*, 16:7373–7387, 2016.
- [4] Wang, Y. et al. Aggravated air pollution events and high secondary aerosol formation potential in the Sichuan Basin, China. *Journal of Geophysical Research: Atmospheres*, 123:4292–4308, 2018.
- [5] Whiteman, C. D. *Mountain Meteorology: Fundamentals and Applications*. Oxford University Press, 2000.
- [6] Ge, C. et al. Validation and calibration of CAMS PM_{2.5} forecasts using in situ PM_{2.5} measurements in China and United States. *Remote Sensing*, 12(22):3813, 2020.
- [7] Ministry of Environmental Protection of the People’s Republic of China. Ambient Air Quality Standards. GB 3095-2012, Beijing, China, 2012.
- [8] Dai, H., Huang, G., Zeng, H., and Yang, F. A Correction Method of Environmental Meteorological Model Based on Long-Short-Term Memory Neural Network. *Earth and Space Science*, 6(12):2423–2434, 2019.
- [9] Qi, H. et al. Multi-model Evaluation and Bayesian Model Averaging in Quantitative Air Quality Forecasting in Central China. *Aerosol and Air Quality Research*, 22(3):210247, 2022.
- [10] Ali, M. A. et al. Accuracy assessment of CAMS and MERRA-2 reanalysis PM_{2.5} and PM₁₀ concentrations over China. *Atmospheric Environment*, 288:119297, 2022.
- [11] Jiang, Y. et al. Contribution of Regional PM2.5 Transport to Air Pollution Enhanced by Sub-Basin Topography: A Modeling Case over Central China. *Atmosphere*, 11(11):1258, 2020.
- [12] Peng, Z., Liu, H., and Ma, X. Improving WRF-Chem PM2.5 predictions by combining data assimilation and deep-learning-based bias correction. *Environment International*, 195:109186, 2024.
- [13] Nguyen, T., Brandstetter, J., Kapoor, A., Gupta, J. K., and Grover, A. ClimaX: a foundation model for weather and climate. In *International Conference on Machine Learning*, 2023.
- [14] Lam, R. et al. Learning skillful medium-range global weather forecasting. *Science*, 382(6677):1416–1421, 2023.
- [15] Bi, K. et al. Accurate medium-range global weather forecasting with 3D neural networks. *Nature*, 619(7970):533–538, 2023.
- [16] Bodnar, C. et al. A foundation model for the Earth system. *Nature*, 641:1180–1181, 2025.
- [17] Dosovitskiy, A. et al. An Image is Worth 16x16 Words: Transformers for Image Recognition at Scale. In *International Conference on Learning Representations*, 2021.
- [18] Liang, J. et al. SwinIR: Image Restoration Using Swin Transformer. In *IEEE/CVF ICCV Workshops*, pages 1833–1844, 2021.
- [19] Vaswani, A. et al. Attention is all you need. In *NeurIPS*, pages 6000–6010, 2017.
- [20] Hettige, K. H. et al. AirPhyNet: Harnessing physics-guided neural networks for air quality prediction. *arXiv preprint arXiv:2402.03784*, 2024.
- [21] Xu, Y. et al. Improving air quality assessment using physics-inspired deep graph learning. *npj Climate and Atmospheric Science*, 6:152, 2023.

[22] Kheder, A., Foreback, B., Wang, L., Liu, Z.-S., and Boy, M. Deep Spatio-Temporal Neural Network for Air Quality Reanalysis. In Petersen, J. and Dahl, V. A., editors, *Image Analysis (SCIA 2025)*, pages 74–87. Springer, 2025.

[23] Nedungadi, V. et al. AirCast: Improving Air Pollution Forecasting Through Multi-Variable Data Alignment. In *ICML 2025 Workshop*, 2025.

[24] Kong, L. et al. A 6-year-long (2013–2018) high-resolution air quality reanalysis dataset in China based on the assimilation of surface observations from CNEMC. *Earth System Science Data*, 13(2):529–570, 2021.

[25] Amante, C. and Eakins, B. W. ETOPO1 1 Arc-Minute Global Relief Model: Procedures, Data Sources and Analysis. NOAA Technical Memorandum NESDIS NGDC-24, 2009.

[26] Center for International Earth Science Information Network (CIESIN). Gridded Population of the World, Version 4 (GPWv4): Population Density, Revision 11. NASA SEDAC, 2018.

[27] OpenAQ. OpenAQ – Open Air Quality Data. <https://openaq.org>, 2024.

[28] Bishop, C. M. *Pattern Recognition and Machine Learning*. Springer, New York, 2006.

[29] Inness, A. et al. The CAMS reanalysis of atmospheric composition. *Atmospheric Chemistry and Physics*, 19(6):3515–3556, 2019.

[30] Wu, C., Li, K., and Bai, K. Validation and Calibration of CAMS PM_{2.5} Forecasts Using In Situ PM_{2.5} Measurements in China and United States. *Remote Sensing*, 12(22):3813, 2020.

[31] Lin, M. et al. Climate variability modulates western US ozone air quality in spring via deep stratospheric intrusions. *Nature Communications*, 6:7105, 2015.

[32] Knowland, K. E. et al. Stratospheric intrusion-influenced ozone air quality exceedances investigated in the NASA MERRA-2 reanalysis. *Geophysical Research Letters*, 44(20):10691–10701, 2017.

[33] Zhao, D. et al. Impact of stratospheric intrusions on ozone enhancement in the lower troposphere and implication to air quality in Hong Kong and other South China regions. *Journal of Geophysical Research: Atmospheres*, 126(3):e2020JD033955, 2021.

[34] Lefohn, A. S. et al. Quantifying the importance of stratospheric-tropospheric transport on surface ozone concentrations at high- and low-elevation monitoring sites in the United States. *Atmospheric Environment*, 62:646–656, 2012.

[35] Kar, J. et al. Evidence of vertical transport of carbon monoxide from MOPITT. *Geophysical Research Letters*, 31(23):L23105, 2004.

[36] Park, M. et al. Transport pathways of carbon monoxide in the Asian summer monsoon diagnosed from MOZART. *Journal of Geophysical Research: Atmospheres*, 114(D8):D08303, 2009.

[37] Foreback, B. et al. A Lagrangian view on severe haze in Beijing: local and long-range sources of trace gases and primary and secondary aerosols. *Atmospheric Environment*, 363:121602, 2025.

[38] Xu, H. et al. Permutation Equivariance of Transformers and its Applications. In *IEEE/CVF CVPR*, pages 5987–5996, 2024.

[39] Wilson, R. Air Pollution, the Automobile, and Public Health. *Environment: Science and Policy for Sustainable Development*, 31(4), 1989.